Stable 25 % Efficiency Inorganic Perovskite/Organic Tandem Solar Cells Enabled by Methoxy-free D-A-D'-A-D Interconnecting Layer

*Jiaxing Huang,[‡a] Ziming Chen,[‡a] Yiheng Zhang,[a] Jing Wang,[*b] Wanqing Cai,[*c] Jing Liu,[c] Qiao Meng,[c] Jie Su,[d] Dongxiang Luo,[e] Yonggang Min,[b] Yuan Li,[*a] and Qifan Xue[*a]*

a. J. Huang, Z. Chen, Y. Zhang, Prof. Y. Li, Prof. Q. Xue
State Key Laboratory of Luminescent Materials and Devices, Institute of Polymer Optoelectronic Materials and Devices, School of Materials Science and Engineering, South China University of Technology, Guangzhou 510640, P. R. China.
Email: celiy@scut.edu.cn, qfxue@scut.edu.cn

b. Prof. J. Wang, Prof. Y. Min
School of Materials and Energy, Guangdong University of Technology, Guangzhou 510006, China
E-mail: jingwang777@gdut.edu.cn

c. Prof. W. Cai, J. Liu, Q. Meng
Faculty of Materials Science, MSU-BIT University, Shenzhen 518172, China
E-mail: wqcai@smbu.edu.cn

d. Prof. J. Su
College of Chemistry and Molecular Engineering, Peking University, Beijing 100871

e. Prof. D. Luo
Huangpu Hydrogen Innovation Center/Guangzhou Key Laboratory for Clean Energy and Materials, School of Chemistry and Chemical Engineering, Guangzhou University, Guangzhou 510006, P. R. China

Keywords: dopant-free, organic hole-transporting materials, inorganic perovskite solar cells, perovskite/organic tandem solar cells

Abstract: Developing dopant-free hole-transporting materials (HTMs) with high hole mobilities is essential to achieve efficient and stable inorganic perovskite solar cells (PVSCs). Herein, two linear organic small molecules IDTT-EtCz and IDTT-PhCz with D–A–D'–A–D configurations are designed and synthesized via two high yield steps, and they are successfully employed as HTMs with effective defect passivation in all-inorganic PVSCs. Notably, the IDTT-PhCz exhibits a deeper highest occupied molecular orbital energy level comparing with that of IDTT-EtCz, along with the enhancement of antioxidant activity towards iodine. Interestingly, IDTT-PhCz with aromatized terminal groups shows significantly increased short contacts and higher hole mobilities than IDTT-EtCz. Furthermore, the IDTT-PhCz has been proven to possess effective surface passivation capability and appropriate energy level alignment at the hole-extraction interface, efficiently suppressing recombination loss and enhancing charge collection. Finally, $CsPbI_3$-based PVSCs with IDTT-PhCz as dopant-free HTM achieve a champion power conversion efficiency (PCE) of 21.0 %, which is one of the highest values reported thus far for all-inorganic PVSCs. The optimized device maintains over 90 % of the initial PCE after 500 hours at 60°C, indicating superior thermal stability. Additionally, the $CsPbI_2Br$ PVSC based on IDTT-PhCz exhibits an impressive PCE of 18.0 %, and a $CsPbI_2Br$/organic tandem solar cell based on IDTT-PhCz achieves a record-high PCE of 25.0 % (24.66 % certified), which is the highest efficiency among the n-i-p perovskite/organic tandem solar cells to date. Overall, this work demonstrates the superiority and generalizability of the D–A–D'–A–D-type design strategy for achieving efficient PVSCs.

1. Introduction

In recent years, all-inorganic cesium lead halide perovskite ($CsPbI_{3-x}Br_x$) solar cells have garnered increasing attention due to their high efficiencies and impressive device stabilities.[1] All-inorganic perovskites remain stable even at 350 °C, attributed to the presence of the inorganic monovalent cesium cation meeting the requirements of ABX_3.[2] In addition, all-inorganic perovskites exhibit superior light-absorption abilities, high carrier mobilities, and efficient solution processabilities.[3] Moreover, their appropriate energy levels (ranging from 1.7 to 2.3 eV[4]) make them suitable for fabricating perovskite/silicon,[5] perovskite/perovskite[6] or perovskite/organic tandem solar cells.[7] Despite achieving power conversion efficiencies (PCEs) higher than 21.0 %, most current inorganic perovskite solar cells rely on the doped HTMs, which can seriously accelerate the degradation of perovskite solar cells (PVSCs).[8] Miyasaka et al. introduced a PDTDT polymer in $CsPbI_2Br$-based PVSCs, achieving a high efficiency of 17.36 % with negligible hysteresis.[9] Fang et al. utilized P3CT-N as an HTM in

$CsPbI_3$-based PVSCs, achieving a PCE of 18.9 %.[10] Hong et al. reported high-efficiency all-inorganic phase-heterojunction solar cells using dimethylammonium iodide-assisted β−$CsPbI_3$ and guanidinium iodide-assisted γ−$CsPbI_3$, with P3HT and SMe-TATPyr as dopant-free HTMs, realizing a PCE of 21.59 %.[11] We have also designed various small-molecule and polymeric HTMs without dopants, such as PSQ, PFBIT, and DTB-FL, and successfully employed them in inorganic PVSCs.[12] However, most inorganic PVSCs with dopant-free HTMs suffer from relatively low PCEs (< 20 %). Hence, it is crucial to develop dopant-free HTMs for all-inorganic PVSCs with PCEs exceeding 20 %.

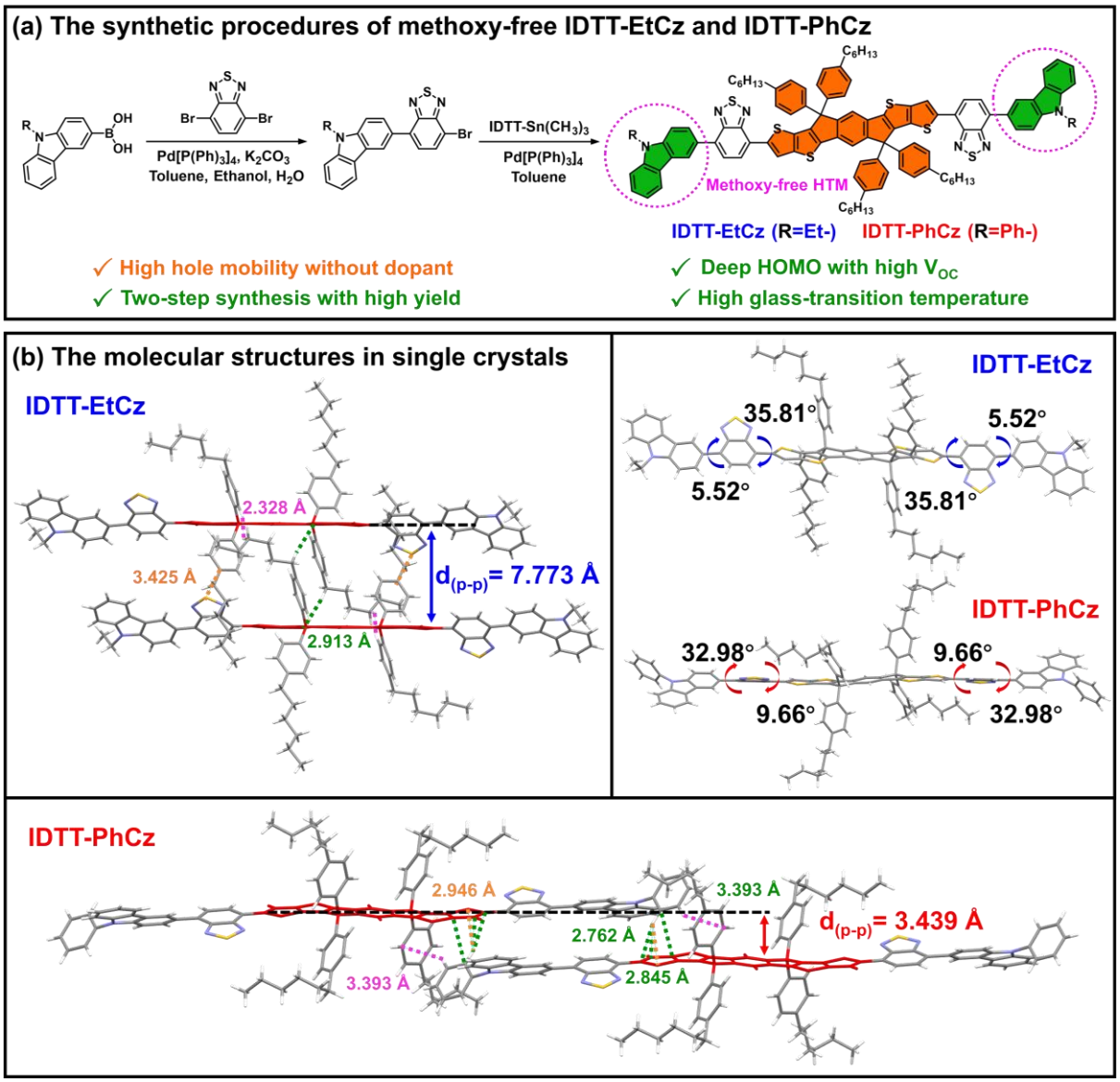

Figure 1. a) Synthesis routes to IDTT-EtCz and IDTT-PhCz. b) Single-crystal structures of IDTT-EtCz and IDTT-PhCz with different packing modes. The green, purple, and orange dotted lines represent the short contacts of ····C–H···π, ···C–H···C–H, and ·····C···S, respectively.

The 2,2′,7,7′-Tetrakis[*N*,*N*′-bis(*p*-methoxyphenyl)amino]-9,9′-spirobifluorene (Spiro-OMeTAD) is widely recognized as an efficient HTM.[8a] However, its effectiveness in PVSC applications relies on hygroscopic dopants (such as Li-TFSI),[13] and the migration of Li^+ ions from the hole-transporting layer (HTL) to other layers can significantly deteriorate device performance.[8] Therefore, there is a pressing need for the development of dopant-free HTMs with straightforward synthetic routes.[14] Linear HTMs with simple geometric structures have been extensively investigated due to their facile synthesis and high PCEs.[15] To date, the design strategies for linear HTMs mainly involve alternating D_1–A–D_2 and D_1–π (D')–D_2 structures,[16] where donor–acceptor (D-A) pairs facilitate strong intramolecular charge transfer (ICT), and the electron-donating π-bridge enhances π–π packing, absorption behaviour, and charge carrier mobility.[16d,17] The methoxy-free donors, such as carbazole, may endow the HTMs with low cost and deep HOMO.[18] Therefore, the design of dopant-free HTM without methoxy groups is crucial for efficient PVSCs.

According to the aforementioned design strategy, methoxy-free D–A–D'–A–D-type HTMs with strong ICT and extended conjugation were synthesized in this study. Two economical and relatively twisted ending groups (EtCz-BT-Br and PCz-BT-Br) were introduced to fabricate dopant-free HTMs (**Figure 1a**). The indacenodithieno[3,2-b]thiophene (IDTT) middle planar π-bridge, along with four alkyl chains, imparted the target HTMs with a relatively large conjugated backbone, high hole mobility, high solubility and high glass-transition temperature (T_g).[18d] These characteristics are beneficial for enhancing the thermal stability of PVSCs, facilitating compact interactions between the HTM-perovskite interface, and reducing charge recombination losses.[12c,19] Additionally, the sulfur atoms in benzothiadiazole (BT) and IDTT are advantageous for passivating under-coordinated lead ions (Pb^{2+}) on the perovskite surface and strengthening the coordination bonding.[12c,19c] Consequently, IDTT-PhCz, featuring a terminal phenyl group, exhibits a deeper highest occupied molecular orbital (HOMO) than IDTT-EtCz (with a terminal ethyl group). Furthermore, the enhanced short contacts of IDTT-PhCz between the end group (phenyl group) and another molecule (e.g. thiophene group) results in improved hole mobility.[12c,20] The utilization of IDTT-PhCz as the dopant-free HTM for $CsPbI_3$-based all-inorganic PVSCs results in a record PCE of 21.0 %, which is among the highest values achieved for all-inorganic PVSCs to date. Moreover, IDTT-PhCz-based PVSCs maintained over 90 % of their initial PCE at 60 °C after 500 hours, demonstrating superior thermal stability. IDTT-PhCz was also employed in $CsPbI_2Br$ PVSCs and conventional perovskite/organic tandem solar cells, achieving record PCEs of 18.0 % and 25.0 % (24.66 %

certified), respectively. These results underscore the considerable potential of the D–A–D'–A–D-type material as an efficient and generalizable HTM for stable PVSCs.[21]

2. Results and discussion

The chemical structures of intermediates and target products were characterized via ^{1}H- and ^{13}C-nuclear magnetic resonance (NMR) spectroscopy, as well as matrix-assisted laser desorption–ionization on a time-of-flight mass spectrometer (MALDI-TOF-MS), with the results presented in **Figures S1–S12**. Two methoxy-free donors, EtCz and PCz, were coupled with the electron acceptor BT via high-yield Suzuki-coupling reactions to construct the intermediates EtCz-BT-Br and PCz-BT-Br, respectively. Subsequently, the various intermediates underwent efficient Stille-coupled with IDTT-tin reagents to yield the target products IDTT-EtCz and IDTT-PhCz, with respective yields of 90.5% and 83.8%. IDTT served as the fused-ring core due to its enhanced conjugation backbone and faster charge transport compared to indacenodithiophene.[22] The π bridge, incorporating two thieno[3,2-*b*]thiophene units, strengthened the coordination bond with the perovskite, endowing the molecular film with high photothermal stability.[19c] A carbazole unit was employed as the terminal group owing to its strong electron-donating capability. The replacement of substituents (ethyl and phenyl) on carbazole allowed for the investigation of the effect of terminal groups on intermolecular stacking and passivation at the perovskite–HTM interface. Notably, the methoxy-free terminal groups of IDTT-PhCz did not contain 4-methoxy-*N*-(4-methoxyphenyl)-*N*-phenylaniline, thereby reducing synthesis costs. The costs of IDTT-PhCz and reported organic small-molecule HTMs are summarized in **Table S6**. Meanwhile, the costs of 1 mL of precursor solutions for IDTT-PhCz and doped Spiro-OMeTAD are recorded in **Tables S3–S5**.

The molecular structures of two HTMs were determined through single-crystal structure analysis. The crystal structure files have been submitted to the Cambridge Crystallographic Data Centre (NO. 2325942 for IDTT-EtCz and NO. 2325944 for IDTT-PhCz), with additional crystallographic details provided in **Tables S7–S22**. The torsion angles of IDTT-PhCz were calculated to be 32.98° for BT with a terminal group and 9.66° for BT with an IDTT core (**Figure 1b**). In contrast, IDTT-EtCz exhibited smaller torsion angles between BT and the terminal group (5.52°), and relatively large torsion angles between BT and IDTT (35.81°), which are not conducive to the improvement of main-chain conjugation and hole mobility. Distinct molecular packing motifs in single crystal were also identified. IDTT-PhCz displays a closer plane-to-plane distances ($d_{p–p}$) of 3.439Å than IDTT-EtCz with a $d_{p–p}$ of 7.773 Å. The tight π-π packing is probably beneficial to achieve faster hole transport. Moreover, the phenyl

group of the end group in IDTT-PhCz displayed concentrated and more short contacts with the thiophene building block on intermediate core of another molecule than IDTT-EtCz (e.g., C–H···π, C–H···C–H, and C···S), which also facilitates efficient hole transport,[20a,20b] and explains the superiority of the phenyl group as the end group in hole transport compared to the ethyl group.

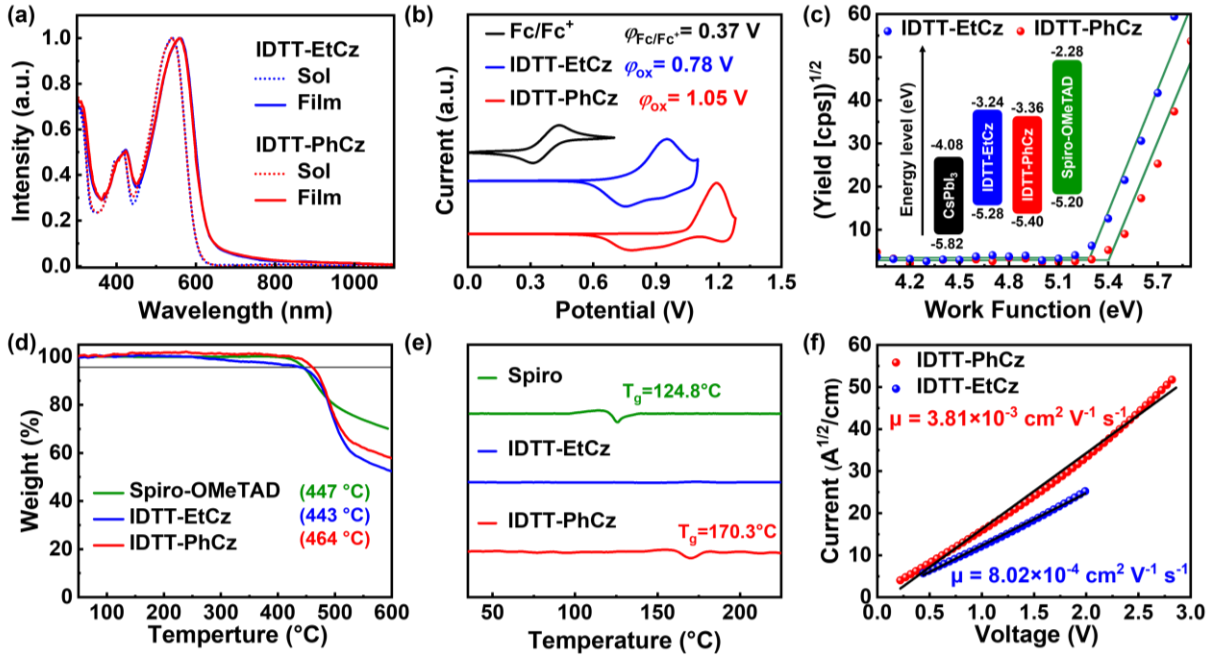

Figure 2. a) The UV–vis–NIR spectra of IDTT-EtCz and IDTT-PhCz in solution (10^{-5} M in DCM) or film state. b) Cyclic voltammetry results of IDTT-EtCz and IDTT-PhCz. The target compounds are coated on a glassy carbon electrode to form the molecular film. An acetonitrile solution containing 0.1 M *n*-Bu_4NPF_6 is adopted as the supporting electrolyte, and the scan rate is 0.05 V s^{-1}. c) Atmospheric photoelectron spectra of IDTT-EtCz and IDTT-PhCz. d) TGA curves of different HTMs at a heating rate of 10 °C/min. e) Differential scanning calorimetry curves of different HTMs. f) V_{OC} versus current for PVSCs with various HTMs.

Table 1. Summary of physical parameters of IDTT-EtCz and IDTT-PhCz.

HTM	λ_{abs} [a] (nm)	E_g^{opt} [b] (eV)	$E_{ox,onset}$ [c] (V)	HOMO [d] (eV)	LUMO [d] (eV)	T_d (°C)	T_g (°C)	μ_0 [e] ($cm^2 V^{-1} s^{-1}$)
IDTT-EtCz	608	2.04	0.78	-5.21	-3.17	443	-	8.02×10^{-4}
IDTT-PhCz	608	2.04	1.05	-5.48	-3.44	464	170.3	3.81×10^{-3}

[a]Measured in the film state; [b]Optical band gaps are obtained from the UV–vis absorption spectra of the spin-coated film via the equation: $E_g^{opt} = 1240/\lambda_{abs}$; [c]$E_{ox,onset}$ represents the onset potential. [d]HOMOs and LUMOs can be calculated via the equations $E_{HOMO} = -(4.8 + E_{ox} - 0.3)$ (eV) and $E_{LUMO} = E_{HOMO} + E_g^{opt}$, respectively. [e]The μ_0 values are evaluated through the classical Mott–Gurney equation $\mu_0 = \frac{8d^3J}{9\varepsilon_0\varepsilon_r V^2}$.

The ultraviolet–visible–near-infrared (UV–vis–NIR) absorption spectra of IDTT-EtCz and IDTT-PhCz are depicted in **Figure 2a**. In both the dichloromethane solution and the thin-film state, the molecules show two characteristic absorption peaks at around 420 and 545 nm, which are consistent with the characteristic absorption of central core and acceptor unit structures. A notable bathochromic shift to 560 nm occurs in the film state due to the enhanced intermolecular π–π stacking effect. The photoluminescence (PL) spectra of the molecules in solution and the thin-film state are shown in **Figure S13**. The PL and UV spectra of IDTT-PhCz and IDTT-EtCz in solution almost overlap. However, the PL emission wavelength of IDTT-PhCz in the film state redshifts to 670 nm, making a 25-nm increase compared with that of IDTT-EtCz (around 645 nm). According to the absorption edges in the film state, the optical bandgaps ($\boldsymbol{E_g^{opt}}$) of IDTT-EtCz and IDTT-PhCz are computed as 2.04 eV. Employing cyclic voltammetry (CV), the initial oxidation potentials of IDTT-EtCz and IDTT-PhCz are determined as 0.78 and 1.05 V, respectively, corresponding to HOMO energy levels of −5.21 eV for IDTT-EtCz and −5.48 eV for IDTT-PhCz (**Figure 2b**), which agrees well with the atmospheric photoelectron spectra findings (−5.28 eV for IDTT-EtCz and −5.40 eV for IDTT-PhCz, **Figure 2c**). The deeper HOMO of IDTT-PhCz may better match the valence band edge position of the perovskite (−5.82 eV) than that of Spiro-OMeTAD (−5.20 eV), thus promoting efficient hole extraction and potentially enhancing the open-circuit voltage (V_{OC}) of PVSCs. The calculations based on the HOMOs and $\boldsymbol{E_g^{opt}}$ yield the lowest unoccupied molecular orbital (LUMO) energy levels of IDTT-EtCz and IDTT-PhCz as −3.17 eV and −3.44 eV, respectively. The optical parameters are listed in **Table 1**, and the energy level diagram is shown in **Figure 2c**.

The thermal properties of Spiro-OMeTAD, IDTT-EtCz, and IDTT-PhCz are studied via thermogravimetric analysis (TGA) and differential scanning calorimetry (DSC). **Figure 2d** presents the decomposition temperatures (T_d) of Spiro-OMeTAD, IDTT-EtCz, and IDTT-PhCz at 5 % weight loss, which are 447 °C, 443 °C, and 464 °C, respectively, highlighting the excellent thermal stability of these small molecules. IDTT-PhCz demonstrates a significantly greater T_d than IDTT-EtCz, indicating that a phenyl terminal group provides stronger thermal stability than an ethyl terminal group. Moreover, IDTT-EtCz exhibits an indistinct phase transition in the DSC measurement (**Figure 2e**), suggesting its relatively stable amorphous forms under inert gas. In contrast, IDTT-PhCz macromolecule displays a high T_g of 170.3 °C, surpassing that of doped Spiro-OMeTAD (72 °C) and pristine Spiro-OMeTAD (124.8 °C)[23], thus ensuring high thermal stability in IDTT-PhCz-based PVSCs. The detailed T_g of reported D-π-D and D-A-D type organic small-molecule HTMs are summarized in **Table S6**.

Both the water contact angles (θ) of IDTT-EtCz and IDTT-PhCz film on indium tin oxide (ITO) exceed 90°, significantly higher than the Spiro-OMeTAD film (72.01°, **Figure 4g**). The increase in θ from IDTT-EtCz (95.01°) to IDTT-PhCz (100.09°) is attributed to the compact packing and additional aromatic rings in the terminal group of IDTT-PhCz.[24] The hydrophobicity and film quality are further demonstrated via transmission electron microscopy (TEM). The Spiro-OMeTAD film exhibits more cracks after contact with water, while the IDTT-EtCz and IDTT-PhCz films remain intact (**Figures 4h** and **S21**). The strong hydrophobicity of IDTT-EtCz and IDTT-PhCz efficiently protect the perovskite films from humidity-induced degradation, thereby enhancing the stability of devices in humid conditions.

The density-functional theory (DFT) calculation was utilized to study the backbone configurations of the two molecules. To simplify the calculation, the alkyl side chains in the IDTT unit were replaced by methyl groups. The calculated molecular geometry (**Figure S14**) reveals that IDTT-PhCz features smaller dihedral angles between the IDTT core, BT, and PCz units than IDTT-EtCz. Notably, IDTT-PhCz exhibits enhanced planarity between the IDTT core and BT unit compared to IDTT-EtCz, as evidenced by the single-crystal structure analysis, which is beneficial for improving intramolecular charge transfer to enhance hole mobility.

The hole-transport behaviour and hole mobility of IDTT-EtCz and IDTT-PhCz films were measured via the space charge-limited current (SCLC) method in the standard device configuration ITO/PEDOT: PSS/HTM/MoO_3/Ag (**Figure 2f**). The measured hole mobilities for IDTT-EtCz and IDTT-PhCz are 8.02×10^{-4} and 3.81×10^{-3} $cm^2\ V^{-1}\ s^{-1}$, respectively. The observed four-fold increase in mobility for IDTT-PhCz compared to IDTT-EtCz is attributed to the tighter packing mode of IDTT-PhCz, facilitating compact π–π stacking and enhancing charge transport capability in the film state. Given the higher hole mobility of IDTT-PhCz, a grazing incident wide-angle X-ray scattering (GIWAXS) analysis was conducted to elucidate the relationship between intermolecular stacking and charge transport properties in response to variations in the terminal group (**Figure S15**). In the in-plane (IP) direction, all films show two weak scattering peaks and a broad peak centered on lamellar packing (q_x = ~0.38 $Å^{-1}$) and π–π stacking (q_x = ~1.56 $Å^{-1}$), which is attributable to the amorphous electron density variation.[12c,19c,25] The similar π–π stacking peak position at q_x = 1.57 $Å^{-1}$ for IDTT-PhCz film and at 1.56 $Å^{-1}$ for IDTT-EtCz film suggests similar packing mode in the film state. In the out-of-plane (OOP) direction, the π–π stacking distance of IDTT-PhCz is 4.00 Å (q_z =1.57 $Å^{-1}$) according to Bragg's law ($d = 2\pi/q$), whereas the IDTT-EtCz film exhibits a larger distance of 4.05 Å (q_z = 1.55 $Å^{-1}$). Overall, all these films exhibit tight stacking effects in the OOP and IP directions, which promotes intermolecular charge transfer and suppressing ionic interdiffusion.

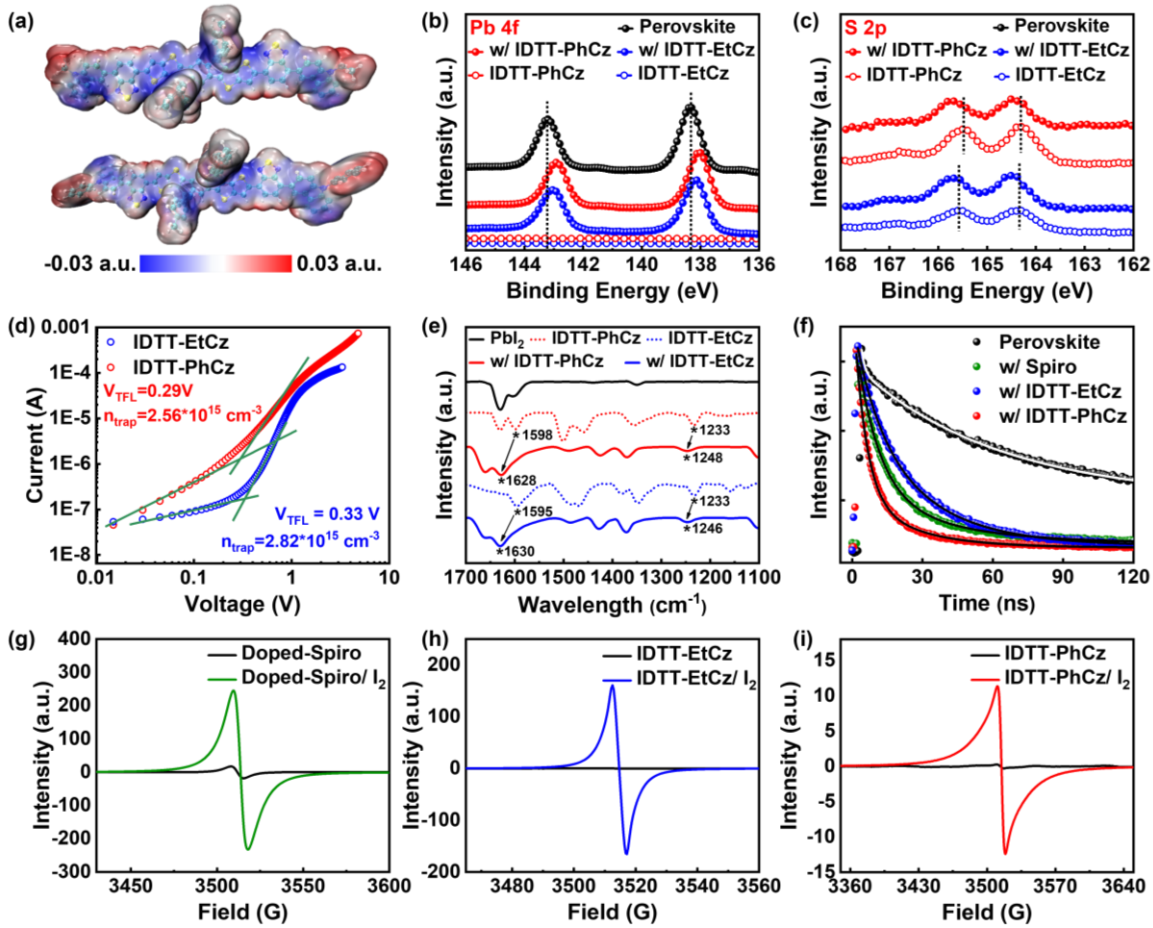

Figure 3. a) ESP potential of IDTT-EtCz (up) and IDTT-PhCz (down) molecules. The red and blue colors indicate positive and negative potentials, respectively. The long alkyl chains are replaced by methyl. b–c) X-ray photoelectron spectroscopy spectra of Pb 4f and S 2p. d) Trap density characterization of the hole-only devices for various HTMs. e) Fourier-transform infrared spectroscopy spectra of HTM, PbI_2, and the PbI_2/HTM blend. f) Time-resolved PL spectra of perovskites with the HTMs of Spiro-OMeTAD, IDTT-EtCz, and IDTT-PhCz. g-i) The electron spin resonance spectra of different HTMs mixed with iodine.

The surface morphology and molecular ordering of Spiro-OMeTAD, IDTT-EtCz, and IDTT-PhCz films were examined using atomic force microscopy (AFM). The root-mean-square (RMS) roughness of Spiro-OMeTAD, IDTT-EtCz, and IDTT-PhCz films coated on ITO are determined as 1.31, 1.13, and 0.68 nm, respectively (**Figure 4i**). Importantly, the RMS of IDTT-PhCz, measuring less than 1 nm, suggests superior film-formation properties than Spiro-OMeTAD and IDTT-EtCz owing to its extended conjugation. Furthermore, thermal stability of the thin films was assessed through heating aging tests. After aging at 100 °C for 100 h in an argon-filled glovebox, Spiro-OMeTAD and IDTT-EtCz exhibited increased roughness (4.37 nm and 3.74 nm, respectively, **Figure S16**), while IDTT-PhCz film showed a slight increase to

1.06 nm. Further aging at 120 °C for 25 h resulted in RMS values exceeding 4 nm for doped Spiro-OMeTAD and IDTT-EtCz films, whereas IDTT-PhCz film maintains a dense and smooth morphology (1.18 nm, **Figure 4i**). This is attributable to the stronger intermolecular interactions provided by the phenyl terminal group than that of the ethyl group, promoting the formation of a tightly stacked thin film and enhancing thermal stability in IDTT-PhCz-based devices.

The electrostatic surface potential (ESP) of HTMs was simulated through DFT, allowing for the study of charge distribution and potential defect passivation effects. The electronegative potentials are predominantly delocalized around the BT and thieno[3,2-*b*]thiophene moieties (**Figure 3a**), suggesting their potential as lewis bases to passivate the undercoordinated Pb^{2+} on the perovskite/HTM interface.[26]

The chemical bonding passivation effects of IDTT-EtCz and IDTT-PhCz on PbI_2 were determined via Fourier-transform infrared spectroscopy (FTIR). In **Figure 3e**, the CH_2-S peak of the thiophene moiety in the IDTT core shifts slightly, from 1233 cm^{-1} to ~1248 cm^{-1} after mixing with PbI_2. Similarly, the C=N stretching peak of the BT unit also shifts from ~1598 cm^{-1} to ~1628 cm^{-1}, indicating effective chemical bond formation between IDTT-EtCz and IDTT-PhCz with PbI_2, thus facilitating perovskite passivation. The interfacial interaction was further confirmed by X-ray photoelectron spectroscopy (XPS, **Figures 3b–3c**). Compared with the pure perovskite sample, IDTT-EtCz- and IDTT-PhCz-based perovskite films exhibit significant shifts in their Pb 4f peaks towards lower binding energies, accompanied by shifts in S 2s peaks towards higher binding energies. This suggests facile electron transfer from S atoms to Pb atoms at the interface upon introducing BT and IDTT with multiple sulfur atoms.[19b,27] The more pronounced peak shift in IDTT-PhCz than that of IDTT-EtCz suggests more efficient donation of lone-pair electrons from S atoms in IDTT-PhCz to the vacant 6p orbital of Pb^{2+} through stronger coordination.[8c,12b] Compared to IDTT-EtCz, the stronger chemical bonding between IDTT-PhCz and Pb^{2+} is advantageous for defect passivation, reducing charge accumulation, and enhancing hole-collection efficiency.

The charge-extraction properties at the perovskite–HTM interfaces were investigated by steady-state PL and time-resolved PL (TRPL) spectroscopy. Perovskite films based on Spiro-OMeTAD, IDTT-EtCz, and IDTT-PhCz exhibited significant PL quenching compared to the pure perovskite film, with IDTT-PhCz showing the most pronounced quenching, representing efficient separation of photogenerated hole-electron pairs and suppression of the recombination process (**Figure S26**).[28] The TRPL decay curves are fitted via the biexponential equation[29]:

$$I(t) = A_1 e^{-\frac{t-t_0}{\tau_1}} + A_2 e^{-\frac{t-t_0}{\tau_2}} \quad \textbf{(1)}$$

where τ_1 and τ_2 represent the fast- and slow-decay time constants, respectively, and A_1 and A_2 are the corresponding decay amplitudes. The lifetime parameters are summarised in **Table S1**. The average lifetime (τ_{ave}) values of pure perovskite, Spiro-OMeTAD, IDTT-EtCz, and IDTT-PhCz film are 58.21, 24.19, 24.90, and 15.43 ns, respectively (**Figure 3f**), aligning well with the PL quenching results. The IDTT-PhCz sample displays the shortest PL decay lifetime, indicating that IDTT-PhCz enables faster hole transfer at the perovskite/HTM interface than IDTT-EtCz. Moreover, the efficient PL quenching and shorter decay lifetime of the IDTT-PhCz film demonstrate that IDTT-PhCz facilitates more efficient hole extraction at the interface than other HTMs, thereby enhancing photovoltaic performance.

The doped Spiro-OMeTAD, dopant-free IDTT-EtCz, and IDTT-PhCz were employed as HTMs to fabricate all-inorganic PVSCs with a structure of glass/ITO/ZnO/SnO_2/$CsPbI_3$/HTM/MoO_3/Ag (**Figure S17**). The optimized current density–voltage (*J*–*V*) curves of the top-performing devices, recorded in both reverse and forward scan directions, are depicted in **Figures 4a** and **S18**. Compared with the Spiro-OMeTAD-based control device (PCE = 19.3 %) and the IDTT-EtCz-based device (PCE = 18.0 %), the IDTT-PhCz-based devices exhibited higher performance (PCE = 21.0 %), with minimal hysteresis under 100 mW cm^{-2} AM 1.5G illumination, a V_{OC} of 1.25 V, a short-circuit photocurrent (J_{SC}) of 20.3 mA cm^{-2}, and a fill factor (FF) of 82.6 %, which rank among the highest-reported values (**Table S25**). The enhanced PCE of the IDTT-PhCz-based device is attributed to the improved charge-transfer ability and reduced charge-recombination loss. The external quantum efficiency (EQE) curves are displayed in **Figure 4b**. IDTT-PhCz exhibits comparable EQE to Spiro-OMeTAD, while IDTT-EtCz displays slightly reduced EQE in the visible light region, potentially leading to a reduction in the J_{SC} of the device. The integrated J_{SC} values obtained from the EQE curves are 20.00, 18.70, and 19.71 mA cm^{-2} for the Spiro-OMeTAD, IDTT-EtCz, and IDTT-PhCz, respectively, consistent with the *J*–*V* measurement results (**Table S2**). The V_{OC} of IDTT-EtCz and IDTT-PhCz devices increase to 1.21 and 1.25 V, respectively, higher than that of the Spiro-OMeTAD-based control device (V_{OC} = 1.19 V), which is related to the deeper HOMO level and enhanced charge-extraction ability at the perovskite–HTM interface of IDTT-PhCz. The statistical distribution of the photovoltaic parameters of 17 devices for all HTMs is shown in **Figure S19**, with detailed values provided in **Table 2**. The results indicate that all the HTM-based devices feature good reliability and repeatability. Additionally, $CsPbI_2Br$-based PVSCs with larger bandgaps were also fabricated, and the *J*–*V* curves are presented in **Figure S20**. IDTT-PhCz-based PVSCs deliver a PCE of 18.0 % with a V_{OC} of 1.33

V, a J_{SC} of 16.5 mA cm^{-2}, and an FF of 82.1 %, making it feasible to combine with low-bandgap organic solar cells to fabricate two-terminal perovskite/organic tandem solar cells.

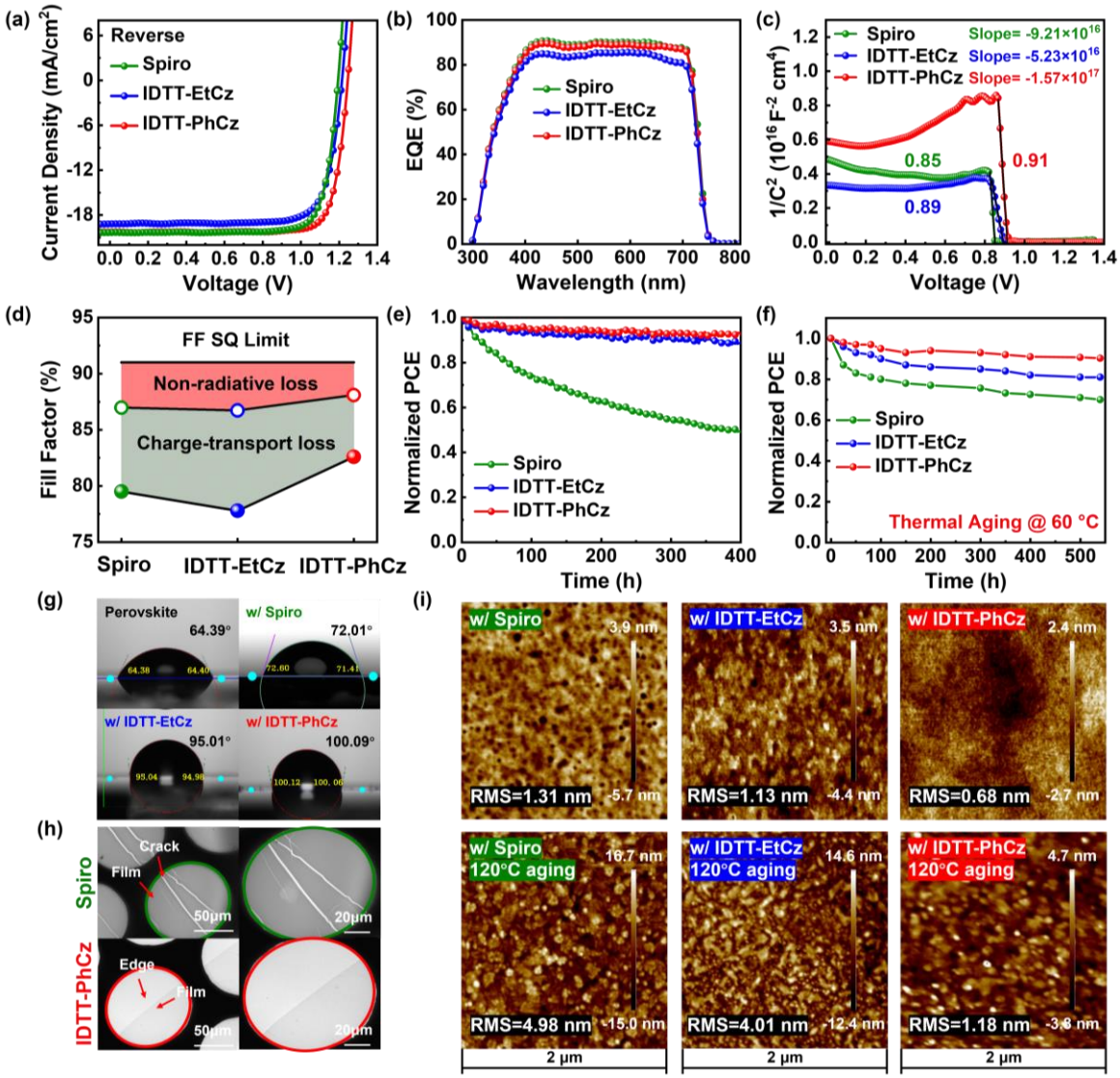

Figure 4. a) J–V curves of the best-performing devices recorded in the reverse scan direction. b) EQE curves of devices with various HTMs. c) Mott–Schottky plots of devices based on various HTMs. d) Fill factor (FF) loss of devices, comprising non-radiative loss and charge-transport loss. The solid and hollow circles represent the measured FF and the maximum FF without charge-transport loss, respectively. e) Continuous maximum power point (MPP) tracking of unencapsulated PVSCs with various HTMs under continuous 1-sun illumination in N_2-filled glovebox. f) Thermal stability of unencapsulated devices based on various HTMs at 60°C. g) The water contact angle of different HTM films on ITO. h) Transmission electron microscopy images of Spiro-OMeTAD and IDTT-PhCz after contact with water. i) Atomic force microscopy images of different HTMs on ITO substrates before and after heating treatment in N_2-filled glovebox.

The steady-state power outputs (SPO) of the best-performing devices under maximum power point (MPP) tracking display negligible PCE losses (**Figure S22**), with the IDTT-PhCz maintaining the highest PCE. Thermal stability measurements are conducted at 60 °C in an argon atmosphere. Remarkably, the IDTT-PhCz-based device exhibits excellent thermal stability (**Figure 4f**), maintaining 90 % of its initial PCE after 540 hours of continuous aging, thereby outperforming the Spiro-OMeTAD- and IDTT-EtCz-based devices, which sustain 70 % and 81 % of their initial PCEs, respectively.

The iodine migration in devices usually corrodes the electrode and leads to a decline in long-term stability.[12c,19c] The electron spin resonance (ESR) spectroscopy was applied to research the interaction between iodine and HTMs (**Figures 3g-i**). The mixture of 0.02 mmol HTM and 0.01 mmol iodine was encapsulated in nuclear magnetic tubes for testing. Both pure IDTT-EtCz and IDTT-PhCz exhibit negligible ESR signals, while the doped Spiro-OMeTAD displays a significant ESR signal due to the generation of Spiro-OMeTAD-based radical cations.[30] After mixing iodine, the spin concentration of all three samples were enhanced, and the ESR signals gradually decreased from doped Spiro-OMeTAD to IDTT-EtCz and then to IDTT-PhCz, showing a gradually increasing antioxidant activity towards iodine. This result is consistent with the gradually decreasing HOMO energy levels of these three samples and indicates that IDTT-EtCz and IDTT-PhCz can significantly retard iodine migration and protect the buried perovskite in the device.

The continuous MPP tracking of unencapsulated PVSCs in nitrogen-filled glove boxes under continuous AM 1.5G illumination is shown in **Figure 4e**. The IDTT-EtCz- and IDTT-PhCz-based devices retain 88 % and 92 % of initial PCEs, respectively, after 400 hours of illumination, while the Spiro-OMeTAD device exhibits significant decay (49 % of its initial PCE). This result demonstrates the improved stability of devices based on the D–A–D'–A–D strategy.

The electrical performances of the devices are studied by conducting capacitance–voltage (*C*–*V*) and electrical impedance spectroscopy (EIS) measurements. The $1/C^2$–*V* plots are obtained through the Mott–Schottky equation[31]:

$$\frac{1}{C^2} = \frac{2}{A^2 e N \varepsilon_0 \varepsilon_r}\left(V_{bi} - V - \frac{2k_B T}{e}\right) \quad (2)$$

where *C*, *A*, *N*, V_{bi}, *V*, k_B, and *T* denote the capacitance of the depletion layer, the active area, the carrier density, the built-in potential at equilibrium, the applied voltage, the Boltzmann's constant, and the absolute temperature, respectively, and the results are shown in **Figure 4c**. The built-in potentials extracted from the intercept of $1/C^2 = 0$ are 0.85, 0.89, and 0.91 V for

Spiro-OMeTAD, IDTT-EtCz, and IDTT-PhCz-based devices, respectively, indicating the augmented driving force for charge separation at the perovskite–IDTT-PhCz interface. Moreover, the charge density at the interface is inversely proportional to the slope value.[32] IDTT-PhCz with a steeper slope compared with the other devices demonstrates accelerated charge transfer and reduced carrier accumulation at the interface.[33] The charge transfer behaviours at the perovskite–HTM interface are examined by EIS. The IDTT-EtCz-, Spiro-OMeTAD-, and IDTT-PhCz-based PVSCs exhibit a gradually increasing charge-recombination resistance in the Nyquist plot (**Figure S23**), revealing improved suppression of charge recombination at the perovskite–HTM interface.[34]

Table 2. Photovoltaic parameters of $CsPbI_3$-based PVSCs with various dopant-free HTMs.

HTM	V_{OC} (V)	J_{SC} (mA cm^{-2})	FF (%)	PCE (%)
Spiro-OMeTAD	1.18 ± 0.01 [a] (1.19)[b]	20.30 ± 0.11 (20.37)	77.9 ± 1.5 (79.5)	18.6 ± 0.5 (19.3)
IDTT-EtCz	1.20 ± 0.01 (1.21)	19.04 ± 0.16 (19.12)	76.9 ± 0.9 (77.8)	17.6 ± 0.3 (18.0)
IDTT-PhCz	1.24 ± 0.01 (1.25)	20.18 ± 0.19 (20.30)	81.3 ± 1.3 (82.6)	20.4 ± 0.5 (21.0)

[a]Average parameter values and standard deviation of 17 devices; [b]parameters of best-performing devices.

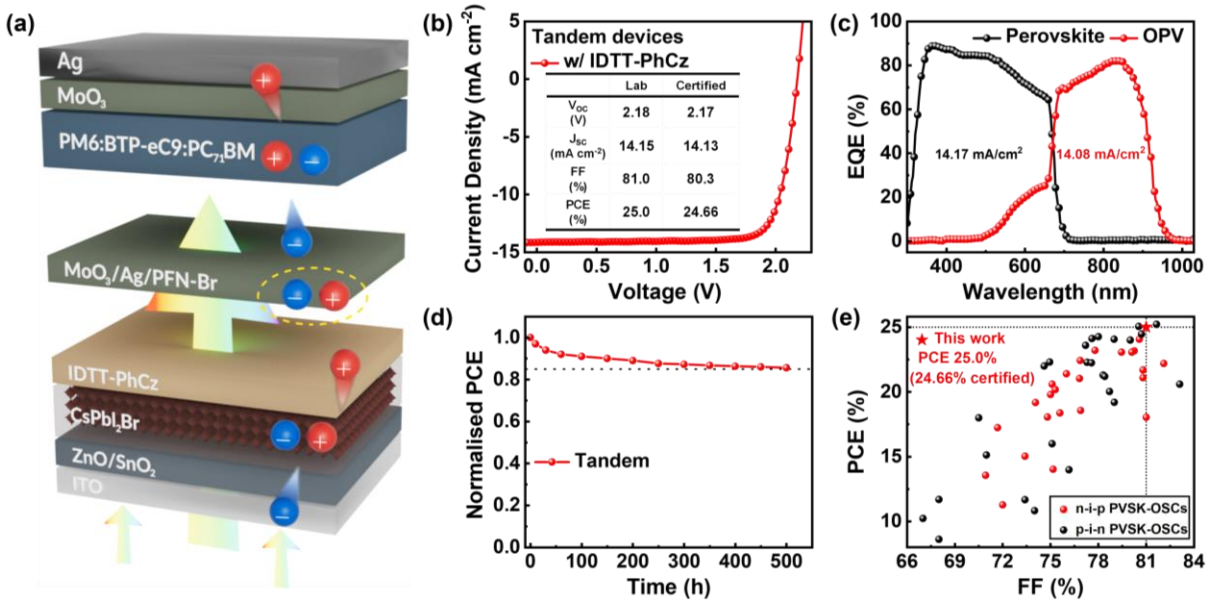

Figure 5. a) Structure of perovskite/organic tandem solar cells. b) J–V characteristics of best-performing tandem solar cells based on IDTT-PhCz as an HTM. The table shows the parameters of the laboratory and certified solar cells. c) EQE curves of tandem solar cells with IDTT-PhCz as HTL. d) Normalised efficiencies of tandem solar cell with IDTT-PhCz as an HTL under continuous 1-sun illumination in N_2-filled glove box. e) PCEs of reported n-i-p or p-i-n perovskite/organic tandem solar cells.

The surface passivation effects of HTMs are studied by hole-only devices with the ITO/PEDOT: PSS/$CsPbI_3$/HTM/MoO_3/Ag structure according to the equation[35]:

$$n_{trap} = \frac{2\varepsilon_0\varepsilon_r V_{TFL}}{eL^2} \quad (3)$$

where V_{TFL}, L, e, ε_r, and ε_0 represent the onset voltage of the trap-filled limit region, the thickness of perovskite films, the elemental charge, the relative dielectric constant, and the vacuum permittivity, respectively. The corresponding trap densities of the IDTT-EtCz- and IDTT-PhCz-based devices are calculated to be 2.82×10^{15} and 2.56×10^{15} cm^{-3}, respectively (**Figure 3d**). Significantly, IDTT-PhCz-based devices exhibit lower trap densities compared to other devices, indicating more efficient passivation of traps at the interface, and consequently reducing non-radiative recombination losses within the device. These results align with the XPS findings, suggesting that IDTT-PhCz, with its enhanced π-π stacking, contributes to defect passivation between S atoms and uncoordinated Pb^{2+}.

In **Figure S24**, the recombination dynamics of the devices are studied via transient photovoltage (TPV) measurements. The charge-recombination lifetimes of Spiro-OMeTAD-, IDTT-EtCz-, and IDTT-PhCz-based devices measured to be 20.8, 17.6, and 29.1 μs, respectively. IDTT-PhCz exhibits a prolonged charge-recombination lifetime in TPV, suggesting its enhanced capability for charge extraction and defect passivation, consequently leading to a reduction in charge recombination losses. These findings are in good agreement with the progressively increasing R_{rec} observed in the EIS spectra of the IDTT-EtCz- to Spiro-OMeTAD- to IDTT-PhCz-based devices, indicating that the perovskite–IDTT-PhCz interface more efficiently suppresses charge recombination and defect passivation compared to other interfaces. Moreover, the relationship between V_{OC} and light intensities (P_{light}) provides insights into the correlation between the charge loss mechanism and photovoltaic performance. The slope of V_{OC} against the natural logarithm of light power offers a deeper understanding of different charge-recombination processes, with a slope closer to 1 indicating less trap-induced recombination in the device.[36] The calculated slopes of Spiro-OMeTAD, IDTT-EtCz, and IDTT-PhCz devices are 1.35, 1.41, and 1.26 k_BT/q, respectively (**Figure S25**), suggesting more effectively suppressed trap-assisted charge recombination at the perovskite/IDTT-PhCz interface compared with other interfaces. This observation is consistent with the trap analysis results.

The underlying mechanisms of FF loss (comprising non-radiative loss and charge-transport loss) in the HTMs are studied through a comparison of the FF loss at the Shockley–Queisser limit and the measured values. The FF loss can be calculated by the following equation:

$$FF_{max} = \frac{V_{OC} - ln(V_{OC} + 0.72)}{V_{OC} + 1} \quad (4)$$

where $V_{OC} = \frac{V_{OC}}{nTk_B/q}$.[37] The IDTT-PhCz-based device demonstrates reduced non-radiative and charge-transport loss compared with the Spiro-OMeTAD- and IDTT-EtCz-based devices (**Figure 4d**). This improvement can be ascribed to the better surface passivation provided by IDTT-PhCz, along with the diminished charge recombination observed in the IDTT-PhCz device compared to the Spiro-OMeTAD and IDTT-EtCz devices.

Furthermore, the $CsPbI_2Br$-based PVSCs with an n-i-p structure are combined with low-bandgap (PM6:BTP-eC9:$PC_{71}BM$)-based organic solar cells to fabricate two-terminal conventional perovskite/organic tandem solar cells. The device structure is illustrated in **Figure 5a**, with IDTT-PhCz serving as the HTL. Remarkably, the tandem device achieves a high PCE of 25.0 % (24.66 % certified, **Figure S27**), with a V_{OC} of 2.18 V, a J_{SC} of 14.15 mA cm^{-2}, and an FF of 81.0 %, making it the highest-PCE devices among reported n-i-p perovskite–organic tandem solar cells (**Figure 5e**, **Tables S23-S24**). The excellent complementary absorption behavior between the two sub cells achieves outstanding EQE (**Figure 5c**), resulting in a higher J_{SC} in the J-V curve (**Figure 5b**) than the other n-i-p perovskite–organic tandem solar cells (**Table S23**). Additionally, the nearly identical integrated densities of 14.17 and 14.08 mA cm^{-2} for both subcells (as listed in **Table S2**) and their alignment with the *J*–*V* curve (14.15 mA cm^{-2}) confirm excellent current matching, which is a critical required for series connections. The tandem solar cell retains 85 % of its initial PCE after continuous operation for 500 hours (**Figure 5d**), highlighting its long-term stability. These results underscore the potential of D–A–D'–A–D-type materials as efficient and generalizable dopant-free HTMs for perovskite photovoltaic devices.

3.Conclusions

In this work, we have synthesized methoxy-free IDTT-EtCz and IDTT-PhCz as dopant-free HTMs for application in PSCs. IDTT-PhCz, featuring a PCz terminal group, aligns closely with the perovskite in terms of energy levels and exhibits tight π–π stacking. This characteristic enhances charge transfer and mitigates charge-recombination losses. Leveraging its excellent surface passivation capability and high hole mobilities, the PVSCs based on $CsPbI_3$ and $CsPbI_2Br$ with IDTT-PhCz as the HTM achieve record-high PCEs of 21.0 % and 18.0 %, respectively. The IDTT-PhCz-based device maintains 90 % of its initial PCE after 500 hours at 60 °C, highlighting its exceptional thermal stability. Moreover, the unencapsulated IDTT-PhCz-based PVSC also retains 92 % of its initial PCE after 400 hours of continuous AM 1.5G

illumination. In addition, IDTT-PhCz serves as an efficient HTM for n-i-p perovskite–organic tandem solar cells. The tandem solar cell based on IDTT-PhCz achieves a remarkable PCE of 25.0 % (certified as 24.66 %), marking the highest reported value to date. The findings of this study underscore the significance of designing D–A–D'–A–D-type HTMs for the development of stable and efficient PVSCs.

Acknowledgements

‡J.H. and Z.C. contributed equally to this work. The work was financially supported by the Shenzhen Pengcheng Peacock Plan Special Hired Position Funding, the National Natural Science Foundation of China (Nos. 22379045, 51973063, 22375065, 62375057, 62074060 and 22405174), the Tip-top Scientific and Technical Innovative Youth Talents of Guangdong Special Support Program (No. 2019TQ05C890), the Guangdong Basic and Applied Basic Research Foundation (Nos. 2021B1515020028, 2020B1515120022, 2022A1515140064 and 2023A0505020011), the Open Research Fund of the Songshan Lake Materials Laboratory (No. 2021SLABFN17), the Guangdong Provincial Key Laboratory of New and Renewable Energy Research and Development (No. E239kf0901), the TCL Young Scholars Program. D. Luo acknowledges support from the Guangdong Basic and Applied Basic Research Foundation (No. 2020B1515020032), the Science and Technology Program of Guangzhou (No. 2023A03J0024), and the Research Project of Guangzhou University (No. ZH2023006).

Conflict of Interest Statement

The authors have no conflicts of interest to declare.

Received: ((will be filled in by the editorial staff))
Revised: ((will be filled in by the editorial staff))
Published online: ((will be filled in by the editorial staff))

References

[1] a) H. Zhang, Q. Tian, W. Xiang, Y. Du, Z. Wang, Y. Liu, L. Liu, T. Yang, H. Wu, T. Nie, W. Huang, A. Najar, S. Liu, *Adv. Mater.* **2023**, *35*, 2301140; b) Q. Tai, K.-C. Tang, F. Yan, *Energy Environ. Sci.* **2019**, *12*, 2375−2405; c) Z. Wang, Z. Shi, T. Li, Y. Chen, W. Huang, *Angew. Chem. Int. Ed.* **2017**, *56*, 1190−1212.

[2] J. Tian, Q. Xue, Q. Yao, N. Li, C. J. Brabec, H.-L. Yip, *Adv. Energy Mater.* **2020**, *10*, 2000183.

[3] a) R. Wang, T. Huang, J. Xue, J. Tong, K. Zhu, Y. Yang, *Nat. Photonics* **2021**, *15*, 411−425; b) K. Wang, S. Ma, X. Xue, T. Li, S. Sha, X. Ren, J. Zhang, H. Lu, J. Ma, S. Guo, Y. Liu, J. Feng, A. Najar, S. Liu, *Adv. Sci.* **2022**, *9*, 2105103; c) X. Gu, W. Xiang, Q. Tian, S. Liu, *Angew. Chem. Int. Ed.* **2021**, *60*, 23164−23170; d) B. Yu, J. Shi, S. Tan, Y. Cui, W. Zhao, H. Wu, Y. Luo, D. Li, Q. Meng, *Angew. Chem. Int. Ed.* **2021**, *60*, 13436−13443; e) X. Chang, J. Fang, Y. Fan, T. Luo, H. Su, Y. Zhang, J. Lu, L. Tsetseris, T. D. Anthopoulos, S. Liu, K. Zhao, *Adv. Mater.* **2020**, *32*, 2001243.

[4] a) J. A. Steele, H. Jin, I. Dovgaliuk, R. F. Berger, T. Braeckevelt, H. Yuan, C. Martin, E. Solano, K. Lejaeghere, S. M. J. Rogge, C. Notebaert, W. Vandezande, K. P. F. Janssen, B. Goderis, E. Debroye, Y.-K. Wang, Y. Dong, D. Ma, M. Saidaminov, H. Tan, Z. Lu, V. Dyadkin, D. Chernyshov, V. Van Speybroeck, E. H. Sargent, J. Hofkens, M. B. J. Roeffaers, *Science* **2019**, *365*, 679−684; b) Q. Wang, X. Zheng, Y. Deng, J. Zhao, Z. Chen, J. Huang, *Joule* **2017**, *1*, 371−382; c) Y. Wang, M. I. Dar, L. K. Ono, T. Zhang, M. Kan, Y. Li, L. Zhang, X. Wang, Y. Yang, X. Gao, Y. Qi, M. Grätzel, Y. Zhao, *Science* **2019**, *365*, 591−595.

[5] a) M. De Bastiani, A. J. Mirabelli, Y. Hou, F. Gota, E. Aydin, T. G. Allen, J. Troughton, A. S. Subbiah, F. H. Isikgor, J. Liu, L. Xu, B. Chen, E. Van Kerschaver, D. Baran, B. Fraboni, M. F. Salvador, U. W. Paetzold, E. H. Sargent, S. De Wolf, *Nat. Energy* **2021**, *6*, 167−175; b) R. Pandey, S. Bhattarai, K. Sharma, J. Madan, A. K. Al-Mousoi, M. K. A. Mohammed, M. K. Hossain, *ACS Appl. Electron. Mater.* **2023**, *5*, 5303−5315; c) F. Fu, J. Li, T. C.-J. Yang, H. Liang, A. Faes, Q. Jeangros, C. Ballif, Y. Hou, *Adv. Mater.* **2022**, *34*, 2106540; d) E. Aydin, T. G. Allen, M. De Bastiani, L. Xu, J. Ávila, M. Salvador, E. Van Kerschaver, S. De Wolf, *Nat. Energy* **2020**, *5*, 851−859; e) J. Werner, B. Niesen, C. Ballif, *Adv. Mater. Interfaces* **2018**, *5*, 1700731.

[6] a) C. Li, Z. Song, C. Chen, C. Xiao, B. Subedi, S. P. Harvey, N. Shrestha, K. K. Subedi, L. Chen, D. Liu, Y. Li, Y.-W. Kim, C.-s. Jiang, M. J. Heben, D. Zhao, R. J. Ellingson, N. J. Podraza, M. Al-Jassim, Y. Yan, *Nat. Energy* **2020**, *5*, 768−776; b) G. E. Eperon, T. Leijtens, K. A. Bush, R. Prasanna, T. Green, J. T.-W. Wang, D. P. McMeekin, G. Volonakis, R. L. Milot, R. May, A. Palmstrom, D. J. Slotcavage, R. A. Belisle, J. B. Patel, E. S. Parrott, R. J. Sutton, W. Ma, F. Moghadam, B. Conings, A. Babayigit, H.-G. Boyen, S. Bent, F. Giustino, L. M. Herz, M. B. Johnston, M. D. McGehee, H. J. Snaith, *Science* **2016**, *354*, 861−865; c) M. Jošt, L. Kegelmann, L. Korte, S. Albrecht, *Adv. Energy Mater.* **2020**, *10*, 1904102; d) Z. Yu, X. Chen, S. P. Harvey, Z. Ni, B. Chen, S. Chen, C. Yao, X.

Xiao, S. Xu, G. Yang, Y. Yan, J. J. Berry, M. C. Beard, J. Huang, *Adv. Mater.* **2022**, *34*, 2110351.

[7] a) K. O. Brinkmann, T. Becker, F. Zimmermann, C. Kreusel, T. Gahlmann, M. Theisen, T. Haeger, S. Olthof, C. Tückmantel, M. Günster, T. Maschwitz, F. Göbelsmann, C. Koch, D. Hertel, P. Caprioglio, F. Peña-Camargo, L. Perdigón-Toro, A. Al-Ashouri, L. Merten, A. Hinderhofer, L. Gomell, S. Zhang, F. Schreiber, S. Albrecht, K. Meerholz, D. Neher, M. Stolterfoht, T. Riedl, *Nature* **2022**, *604*, 280−286; b) W. Chen, Y. Zhu, J. Xiu, G. Chen, H. Liang, S. Liu, H. Xue, E. Birgersson, J. W. Ho, X. Qin, J. Lin, R. Ma, T. Liu, Y. He, A. M.-C. Ng, X. Guo, Z. He, H. Yan, A. B. Djurišić, Y. Hou, *Nat. Energy* **2022**, *7*, 229−237; c) Y. Ding, Q. Guo, Y. Geng, Z. Dai, Z. Wang, Z. Chen, Q. Guo, Z. Zheng, Y. Li, E. Zhou, *Nano Today* **2022**, *46*, 101586; d) S. Qin, C. Lu, Z. Jia, Y. Wang, S. Li, W. Lai, P. Shi, R. Wang, C. Zhu, J. Du, J. Zhang, L. Meng, Y. Li, *Adv. Mater.* **2022**, *34*, 2108829.

[8] a) L. Nakka, Y. Cheng, A. G. Aberle, F. J. A. E. Lin, S. Research, *Adv. Energy Sustainability Res.* **2022**, *3*, 2200045; b) J. Wang, X. Wu, Y. Liu, T. Qin, K. Zhang, N. Li, J. Zhao, R. Ye, Z. Fan, Z. J. A. E. M. Chi, *Adv. Energy Mater.* **2021**, *11*, 2100967; c) K. Jiang, J. Wang, F. Wu, Q. Xue, Q. Yao, J. Zhang, Y. Chen, G. Zhang, Z. Zhu, H. Yan, L. Zhu, H.-L. Yip, *Adv. Mater.* **2020**, *32*, 1908011.

[9] Z. Guo, A. K. Jena, I. Takei, M. Ikegami, A. Ishii, Y. Numata, N. Shibayama, T. Miyasaka, *Adv. Funct. Mater.* **2021**, *31*, 2103614.

[10] S. Fu, W. Zhang, X. Li, J. Guan, W. Song, J. Fang, *ACS Energy Lett.* **2021**, *6*, 3661−3668.

[11] S. S. Mali, J. V. Patil, J.-Y. Shao, Y.-W. Zhong, S. R. Rondiya, N. Y. Dzade, C. K. Hong, *Nat. Energy* **2023**, *8*, 989−1001.

[12] a) Y. Bai, Z. Zhou, Q. Xue, C. Liu, N. Li, H. Tang, J. Zhang, X. Xia, J. Zhang, X. Lu, C. J. Brabec, F. Huang, *Adv. Mater.* **2022**, *34*, 2110587; b) Q. Xiao, J. Tian, Q. Xue, J. Wang, B. Xiong, M. Han, Z. Li, Z. Zhu, H.-L. Yip, Z. a. Li, *Angew. Chem. Int. Ed.* **2019**, *58*, 17724−17730; c) T. Niu, W. Zhu, Y. Zhang, Q. Xue, X. Jiao, Z. Wang, Y.-M. Xie, P. Li, R. Chen, F. Huang, Y. Li, H.-L. Yip, Y. Cao, *Joule* **2021**, *5*, 249−269.

[13] Y. Wang, X. Liu, T. Zhang, X. Wang, M. Kan, J. Shi, Y. Zhao, *Angew. Chem. Int. Ed.* **2019**, *131*, 16844−16849.

[14] a) X. Yin, Z. Song, Z. Li, W. Tang, *Energy Environ. Sci.* **2020**, *13*, 4057−4086; b) J. Urieta-Mora, I. García-Benito, A. Molina-Ontoria, N. Martín, *Chem. Soc. Rev.* **2018**, *47*, 8541−8571; c) L. Zhang, X. Zhou, C. Liu, X. Wang, B. Xu, *Small Methods* **2020**, *4*, 2000254.

[15] H. D. Pham, T. C. J. Yang, S. M. Jain, G. J. Wilson, P. Sonar, *Adv. Energy Mater.* **2020**, *10*, 1903326.

[16] a) Y. Chen, X. Xu, N. Cai, S. Qian, R. Luo, Y. Huo, S. W. Tsang, *Adv. Energy Mater.* **2019**, *9*, 1901268; b) Y. Cao, Y. Li, T. Morrissey, B. Lam, B. O. Patrick, D. J. Dvorak, Z. Xia, T. L. Kelly, C. P. Berlinguette, *Energy Environ. Sci.* **2019**, *12*, 3502−3507; c) D. Zhang, P. Xu, T. Wu, Y. Ou, X. Yang, A. Sun, B. Cui, H. Sun, Y. Hua, *J. Mater. Chem. A* **2019**, *7*, 5221−5226; d) P. Xu, P. Liu, Y. Li, B. Xu, L. Kloo, L. Sun, Y. Hua, *ACS Appl. Mater. Interfaces.* **2018**, *10*, 19697−19703; e) F. Wu, Y. Ji, C. Zhong, Y. Liu, L. Tan, L. Zhu, *Chem. Commun.* **2017**, *53*, 8719−8722.

[17] a) Z. a. Li, Z. Zhu, C.-C. Chueh, S. B. Jo, J. Luo, S.-H. Jang, A. K. Y. Jen, *J. Am. Chem. Soc.* **2016**, *138*, 11833−11839; b) H. Zhang, Y. Wu, W. Zhang, E. Li, C. Shen, H. Jiang, H. Tian, W. H. Zhu, *Chem. Sci.* **2018**, *9*, 5919−5928; c) X. Yang, H. Wang, B. Cai, Z. Yu, L. J. J. o. e. c. Sun, *J. Energy Chem.* **2018**, *27*, 650−672.

[18] a) J. Liu, H. Zhang, B. Wu, L. Sun, Y. Chen, X. Zong, Z. Sun, S. Xue, M. Liang, *Sol. RRL* **2021**, *5*, 2100694; b) J. Wang, H. Zhang, B. Wu, Z. Wang, Z. Sun, S. Xue, Y. Wu, A. Hagfeldt, M. Liang, *Angew. Chem. Int. Ed.* **2019**, *58*, 15721−15725; c) H. Yao, T. Wu, B. Wu, H. Zhang, Z. Wang, Z. Sun, S. Xue, Y. Hua, M. Liang, *J. Mater. Chem. A* **2021**, *9*, 8598−8606; d) Y. Xue, Y. Wu, Y. Li, *J. Power Sources* **2017**, *344*, 160−169.

[19] a) H. D. Pham, H. Hu, F.-L. Wong, C.-S. Lee, W.-C. Chen, K. Feron, S. Manzhos, H. Wang, N. Motta, Y. M. Lam, P. Sonar, *J. Mater. Chem. C* **2018**, *6*, 9017−9029; b) Y. Wang, Q. Liao, J. Chen, W. Huang, X. Zhuang, Y. Tang, B. Li, X. Yao, X. Feng, X. Zhang, M. Su, Z. He, T. J. Marks, A. Facchetti, X. Guo, *J. Am. Chem. Soc.* **2020**, *142*, 16632−16643; c) L. Yuan, W. Zhu, Y. Zhang, Y. Li, C. C. S. Chan, M. Qin, J. Qiu, K. Zhang, J. Huang, J. Wang, H. Luo, Z. Zhang, R. Chen, W. Liang, Q. Wei, K. S. Wong, X. Lu, N. Li, C. J. Brabec, L. Ding, K. Yan, *Energy Environ. Sci.* **2023**, *16*, 1597−1609; d) Q. Cheng, H. Chen, F. Yang, Z. Chen, W. Chen, H. Yang, Y. Shen, X.-M. Ou, Y. Wu, Y. Li, Y. Li, *Angew. Chem. Int. Ed.* **2022**, *61*, e202210613; e) Q. Cheng, H. Chen, W. Chen, J. Ding, Z. Chen, Y. Shen, X. Wu, Y. Wu, Y. Li, Y. Li, *Angew. Chem. Int. Ed.* **2023**, *62*, e202312231; f) Q. Cheng, W. Chen, Y. Li, Y. Li, *Adv. Sci.* **2024**, *11*, 2307152.

[20] a) D. Gao, J. Andeme Edzang, A. K. Diallo, T. Dutronc, T. S. Balaban, C. Videlot-Ackermann, E. Terazzi, G. Canard, *New J. Chem.* **2015**, *39*, 7140−7146; b) S. Spencer, H. Hu, Q. Li, H.-Y. Ahn, M. Qaddoura, S. Yao, A. Ioannidis, K. Belfield, C. J. Collison, *Prog. Photovoltaics* **2014**, *22*, 488−493; c) N. J. Hestand, F. C. Spano, *Chem. Rev.* **2018**, *118*, 7069−7163.

[21] G. Xie, J. Wang, S. Yin, A. Liang, W. Wang, Z. Chen, C. Feng, J. Yu, X. Liao, Q. Xue, Y. Fu, Y. Min, X. Lu, Y. Chen, *Angew. Chem. Int. Ed.* **2024**, *63*, e202403083.

[22] a) Y.-X. Xu, C.-C. Chueh, H.-L. Yip, F.-Z. Ding, Y.-X. Li, C.-Z. Li, X. Li, W.-C. Chen, A. K.-Y. Jen, *Adv. Mater.* **2012**, *24*, 6356−6361; b) J. J. Intemann, K. Yao, F. Ding, Y. Xu, X. Xin, X. Li, A. K.-Y. Jen, *Adv. Funct. Mater.* **2015**, *25*, 4889−4897.

[23] a) V. A. Chiykowski, Y. Cao, H. Tan, D. P. Tabor, E. H. Sargent, A. Aspuru-Guzik, C. P. Berlinguette, *Angew. Chem. Int. Ed.* **2018**, *57*, 15529−15533; b) T. Malinauskas, D. Tomkute-Luksiene, R. Sens, M. Daskeviciene, R. Send, H. Wonneberger, V. Jankauskas, I. Bruder, V. Getautis, *ACS Appl. Mater. Interfaces.* **2015**, *7*, 11107−11116.

[24] a) H. Guo, H. Zhang, C. Shen, D. Zhang, S. Liu, Y. Wu, W.-H. Zhu, *Angew. Chem. Int. Ed.* **2021**, *60*, 2674−2679; b) Y. Wang, W. Chen, L. Wang, B. Tu, T. Chen, B. Liu, K. Yang, C. W. Koh, X. Zhang, H. Sun, G. Chen, X. Feng, H. Y. Woo, A. B. Djurišić, Z. He, X. Guo, *Adv. Mater.* **2019**, *31*, 1902781.

[25] Y. Zhao, T. Heumueller, J. Zhang, J. Luo, O. Kasian, S. Langner, C. Kupfer, B. Liu, Y. Zhong, J. Elia, A. Osvet, J. Wu, C. Liu, Z. Wan, C. Jia, N. Li, J. Hauch, C. J. Brabec, *Nat. Energy* **2022**, *7*, 144−152.

[26] Y. Lin, L. Shen, J. Dai, Y. Deng, Y. Wu, Y. Bai, X. Zheng, J. Wang, Y. Fang, H. Wei, W. Ma, X. C. Zeng, X. Zhan, J. Huang, *Adv. Mater.* **2017**, *29*, 1604545.

[27] Q.-Q. Ge, J.-Y. Shao, J. Ding, L.-Y. Deng, W.-K. Zhou, Y.-X. Chen, J.-Y. Ma, L.-J. Wan, J. Yao, J.-S. Hu, Y.-W. Zhong, *Angew. Chem. Int. Ed.* **2018**, *57*, 10959−10965.

[28] Y.-M. Xie, Z. Zeng, X. Xu, C. Ma, Y. Ma, M. Li, C.-S. Lee, S.-W. Tsang, *Small* **2020**, *16*, 1907226.

[29] a) Q. Yao, Q. Xue, Z. Li, K. Zhang, T. Zhang, N. Li, S. Yang, C. J. Brabec, H.-L. Yip, Y. Cao, *Adv. Mater.* **2020**, *32*, 2000571; b) T. Niu, J. Lu, X. Jia, Z. Xu, M.-C. Tang, D. Barrit, N. Yuan, J. Ding, X. Zhang, Y. Fan, T. Luo, Y. Zhang, D.-M. Smilgies, Z. Liu, A. Amassian, S. Jin, K. Zhao, S. Liu, *Nano Lett.* **2019**, *19*, 7181−7190.

[30] F. Cao, Z. Zhu, C. Zhang, P. Chen, S. Wang, A. Tong, R. He, Y. Wang, W. Sun, Y. Li, J. Wu, *Small* **2023**, *19*, 2207784.

[31] Zi'an Zhou, Xianfu Zhang, Rahim Ghadari, Xuepeng Liu, Wenjun Wang, Yong Ding, Molang Cai, Jia Hong Pan, S. Dai, *Sol. Energy* **2021**, *221*, 323−331.

[32] Y. Liu, M. Bag, L. A. Renna, Z. A. Page, P. Kim, T. Emrick, D. Venkataraman, T. P. Russell, *Adv. Energy Mater.* **2016**, *6*, 1501606.

[33] a) O. Almora, C. Aranda, E. Mas-Marzá, G. Garcia-Belmonte, *Appl. Phys. Lett.* **2016**, *109*, 173903; b) T. Bu, J. Li, F. Zheng, W. Chen, X. Wen, Z. Ku, Y. Peng, J. Zhong, Y.-B. Cheng, F. Huang, *Nat. Commun.* **2018**, *9*, 4609.

[34] a) T. Niu, J. Lu, M.-C. Tang, D. Barrit, D.-M. Smilgies, Z. Yang, J. Li, Y. Fan, T. Luo, I. McCulloch, A. Amassian, S. Liu, K. Zhao, *Energy Environ. Sci.* **2018**, *11*, 3358−3366; b) D. Yang, R. Yang, K. Wang, C. Wu, X. Zhu, J. Feng, X. Ren, G. Fang, S. Priya, S. Liu, *Nat. Commun.* **2018**, *9*, 3239.

[35] R. H. Bube, *J. Appl. Phys.* **2004**, *33*, 1733−1737.

[36] G.-J. A. H. Wetzelaer, M. Scheepers, A. M. Sempere, C. Momblona, J. Ávila, H. J. Bolink, *Adv. Mater.* **2015**, *27*, 1837−1841.

[37] a) M. A. Green, *Sol. Cells* **1982**, *7*, 337−340; b) J. Wang, Y. Huang, T. Li, H. Shi, M. He, X. Cheng, S. Ni, C. Zhang, *Arch. Environ. Contam. Toxicol.* **2020**, *79*, 177−183.

Table of contents entry

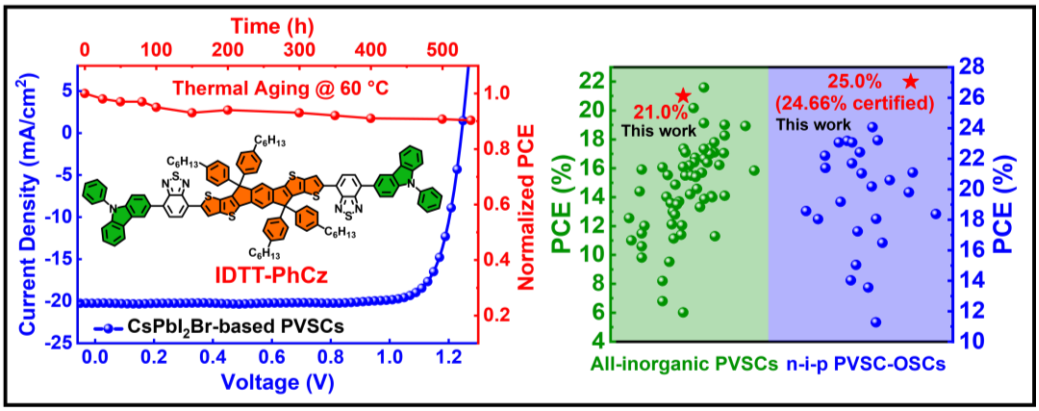

IDTT-PhCz with D–A–D'–A–D configuration is utilized as a dopant-free HTM for all-inorganic PVSCs. The improved defect passivation and short contacts lead to remarkable efficiencies of 21.0 % and 18 % in $CsPbI_3$ and $CsPbI_2Br$ PVSCs, respectively. Moreover, the n-i-p perovskite/organic tandem solar cells with IDTT-PhCz as dopant-free HTM achieve record-high PCEs of 25.0 % (24.66 % certified), which is the highest values reported to date.